

Upscaling of solute plumes in periodic porous media through a trajectory based spatial Markov model

Bianchi Janetti Emanuela¹, Sherman Thomas², Guedon Gael Raymond³, Bolster Diogo², and Porta Giovanni Michele³

¹Politecnico di Milano, Italy

²University of Notre Dame

³Politecnico di Milano

November 16, 2022

Abstract

We propose an approach to upscale solute transport in spatially periodic porous media. Our methodology relies on pore scale information to predict large scale transport features, including explicit reconstruction of the solute plume, breakthrough curves at fixed distances, and spatial spreading transverse to the main flow direction. The proposed approach is grounded on the recently proposed trajectory-based Spatial Markov model (tSMM), which upscales transport based on information collected from advective-diffusive particle trajectories across one periodic element. In previous works, this model has been applied solely to one-dimensional transport in a single periodic pore geometry. In this work we extend the tSMM to the prediction of multi-dimensional solute plumes. This is obtained by analyzing the joint space-time probability distribution associated with discrete particles, as yielded by the tSMM. By comparing numerical results from fully resolved simulations and predictions obtained with the tSMM over a wide range of Péclet numbers, we demonstrate that the proposed approach is suitable for modeling transport of conservative and linearly decaying solute species in a realistic pore space and showcase the applicability of the model to predict steady state solute plumes. Additionally, we evaluate the model performance as a function of numerical parameters employed in the tSMM parameterization.

1 Upscaling of solute plumes in periodic porous media
2 through a trajectory based spatial Markov model

3 Emanuela Bianchi Janetti^a, Thomas Sherman^b, Gaël Raymond Guédon^c,
4 Diogo Bolster^b, Giovanni Porta^a

5 ^a*Dipartimento di Ingegneria Civile ed Ambientale, Politecnico di Milano, Milano, Italy*

6 ^b*Dept. of Civil and Environmental Engineering and Earth Sciences, University of Notre
7 Dame, IN, USA*

8 ^c*Dipartimento di Energia, Politecnico di Milano, Milano, Italy*

9 **Abstract**

We propose an approach to upscale solute transport in spatially periodic porous media. Our methodology relies on pore scale information to predict large scale transport features, including explicit reconstruction of the solute plume, breakthrough curves at fixed distances, and spatial spreading transverse to the main flow direction. The proposed approach is grounded on the recently proposed trajectory-based Spatial Markov model (tSMM), which up-scales transport based on information collected from advective-diffusive particle trajectories across one periodic element. In previous works, this model has been applied solely to one-dimensional transport in a single periodic pore geometry. In this work we extend the tSMM to the prediction of multi-dimensional solute plumes. This is obtained by analyzing the joint space-time probability distribution associated with discrete particles, as yielded by the tSMM. By comparing numerical results from fully resolved simulations and predictions obtained with the tSMM over a wide range of Péclet numbers, we demonstrate that the proposed approach is suitable for modeling transport

of conservative and linearly decaying solute species in a realistic pore space and showcase the applicability of the model to predict steady state solute plumes. Additionally, we evaluate the model performance as a function of numerical parameters employed in the tSMM parameterization.

10 *Keywords:* Upscaling, Porous Media, Transport, Spatial Markov Model,
11 Transverse dispersion

12 **1. Introduction**

13 Solute transport in porous media is a fundamental problem across many
14 disciplines, including subsurface geological systems and the performance op-
15 timization of engineered materials such as filtration membranes. A key chal-
16 lenge in this context is to obtain accurate predictions at spatial scales much
17 larger than the ones associated with individual pores without having to re-
18 solve the physical and chemical processes taking place within complex pore
19 spaces. This is achieved by upscaled formulations that embed pore scale
20 features into effective parameters and therefore can be employed to predict
21 large scale behaviors. To this end, a classical approach is resorting to a
22 continuum-scale advection-dispersion equation (ADE) [1, 2]. In such a for-
23 mulation mechanical dispersion induced by pore scale velocity gradients is
24 modelled through a Fickian-like dispersion term, parameterized via a fourth-
25 rank dispersivity tensor. The definition of the dispersivity tensor purely
26 based on pore scale properties presents significant challenges. From a theo-
27 retical perspective, the solution of three closure problems is required to fully
28 parameterize solute transport based on pore scale information through vol-
29 ume averaging [3]. These separate closures are necessary to isolate and char-

30 acterize the separate effects of diffusion and advection on transport. However,
31 even such a detailed approach may not yield reliable predictions due to a lack
32 of separation of scales, violating the assumptions required by the volume
33 averaging method. In such a case, non-Fickian transport features emerge,
34 particularly at relatively short times and distances [4, 5]. Formally, these
35 effects can still be represented with Eulerian nonlocal (integro-differential)
36 models. In principle these models can be derived by applying upscaling ap-
37 proaches, such as volume averaging, that can relate pore scale geometry and
38 fluid velocities with the emerging transport dynamics through a set of clo-
39 sure differential equations [6]. However, it is often found that resorting to
40 such approaches leads to formidable mathematical and numerical complexity
41 [7, 8], which is associated with *i*) the numerical resolution of various closure
42 problems and *ii*) the approximation of integro-differential equations to obtain
43 the desired large scale outputs.

44 A specific problem in the context of solute transport upscaling is posed
45 by the modeling of solute plumes, which correspond to the explicit spatial
46 reconstruction of the solute spatial spread at a given time, or at steady state
47 (i.e., under steady state boundary conditions, such as continuous injection).
48 For instance, the analysis of transverse spreading and mixing of steady state
49 solute plumes has great practical relevance in bioremediation and reactive
50 transport scenarios at field and laboratory scales [9, 10, 11]. In these ap-
51 plications the target process is the spreading and mixing of a solute in the
52 direction transverse to a steady flow field characterized by a prevalent direc-
53 tion. Following classical ADE-based descriptions, transport in the transverse
54 direction is typically modeled by introducing a dispersivity parameter. This

55 standard definition typically considers dispersion to be uniquely proportional
56 to advective velocity [1]. This formulation was successfully employed, for ex-
57 ample to interpret transport and mixing in microfluidic systems characterized
58 by relatively simple geometries [12]. However, studies performed in the last
59 decade have demonstrated the impact of molecular diffusion on transverse
60 dispersion through experiments and numerical simulations [10, 13, 14, 15].
61 Such results can be qualitatively linked with analytical and numerical stud-
62 ies showing that the dispersion tensor becomes asymmetric in advection-
63 dominated scenarios [16, 17]. These studies show that full parameterization
64 of the dispersion tensor can become a troublesome task, particularly in media
65 characterized by a complex and multi-scale pore structure. Additional levels
66 of complexity are introduced when reactive processes are also considered on
67 top of pore scale advective-diffusive transport.

68 Over the last decade it has been recognized that pore-to-continuum up-
69 scaling of solute transport can often be conveniently obtained by considering
70 solute velocities (or associated travel times) over fixed spatial increments by
71 means of a Markov chain. This led to the formulation of various flavours
72 of so-called Spatial Markov models [e.g. 18, 19, 20, 21]. The SMM is based
73 on the calculation of the travel time across a fixed distance and a one step
74 correlation existing between successive travel times. By including correla-
75 tion the SMM is able to employ information available on a limited portion
76 of the system to predict transport across much larger distances. Notably
77 such an approach is effective in the presence of advection-dominated scenar-
78 ios that become challenging to upscale with classical Eulerian approaches.
79 The advantages of employing a spatial Markov approach to obtain the solute

80 breakthrough curve (or first passage time) at a given longitudinal distance has
81 been demonstrated in a number of previous works, relying on both numerical
82 and laboratory scale experimental datasets [e.g. 18, 21, 22, 23]. Several re-
83 cent works have discussed methodologies that employ Lagrangian SMM-like
84 approaches to predict solute particles' space-time locations at various scales
85 of observations [24, 25]. Yet, to the best of our knowledge, this approach has
86 not been applied to the explicit space-time reconstruction of solute plumes
87 starting from pore scale properties. In this work we present a methodology to
88 upscale transport of solute plumes in the longitudinal and transverse direc-
89 tion via a SMM. We consider periodic media, which are routinely considered
90 as model porous media in theoretical approaches and are employed in engi-
91 neering systems across a wide range of applications [26, 27, 28, 29]. Our work
92 starts from a recently proposed trajectory-based SMM (here labelled tSMM)
93 to upscale transport, mixing and surface reactions across porous media made
94 up of periodic elements [30, 31]. To date, the tSMM has been constrained to
95 a highly idealized setting, a periodic wavy channel, which while it displays
96 some characteristics of real porous media cannot represent their full com-
97 plexity, such as transverse flow or complex pore size distributions. Building
98 on this, we analyze longitudinal and transverse transport within a realis-
99 tic two-dimensional porous domain. Briefly, the specific objectives of this
100 contribution are to *i*) extend the tSMM to the case of a multi-dimensional
101 unsteady solute transport and *ii*) yield an efficient and accurate representa-
102 tion of transient and steady state solute plumes in porous media based on the
103 multi-dimensional tSMM. This second goal entails a specific methodological
104 challenge, as steady state plumes are typically computationally expensive to

105 simulate with Lagrangian particle-based approaches. Our objective is the
 106 development of an upscaled, parsimonious and computationally affordable
 107 particle-based model for this specific configuration.

108 2. Methodology

109 2.1. Pore scale setting

110 We consider transport of a passive solute in a periodic two-dimensional
 111 porous medium. The medium is composed of a collection of periodic unit
 112 cells, whose geometry is represented in Figure 1. The unit cell is artificially
 113 created using a stochastic generation procedure as detailed in [21, 32, 33].
 The cell properties are reported in Table 1. We assume here to deal with

Porosity	L_x [m]	L_y [m]	Δ [m]	ℓ_S [m]
0.631	4.096×10^{-3}	4.096×10^{-3}	2×10^{-6}	1×10^{-4}

Table 1: Geometrical characteristics of the unit cell

114

115 a semi-infinite periodic porous domain, i.e. $x \in [0, \infty)$ and $y \in (-\infty, +\infty)$.
 116 Because the medium is composed by an infinite number of identical cells, for
 117 convenience we define

$$\hat{x} = x - L_x \text{floor} \left(\frac{x}{L_x} \right), \quad \hat{y} = y + \frac{L_y}{2} - L_y \text{floor} \left(\frac{y}{L_y} + \frac{1}{2} \right) \quad (1)$$

118 as a coordinate system referenced to the unit cell, $\hat{x} \in [0, L_x]$ and $\hat{y} \in [0, L_y]$,
 119 where L_x and L_y define the dimensions of the unit cell in the x - and y -
 120 directions, respectively. The cell is discretized into square pixels of side
 121 $\Delta = 2 \times 10^{-6}$ m, which for our example results in a unit cell composed of
 122 2048×2048 pixels. The solid and fluid phases are identified by an indicator

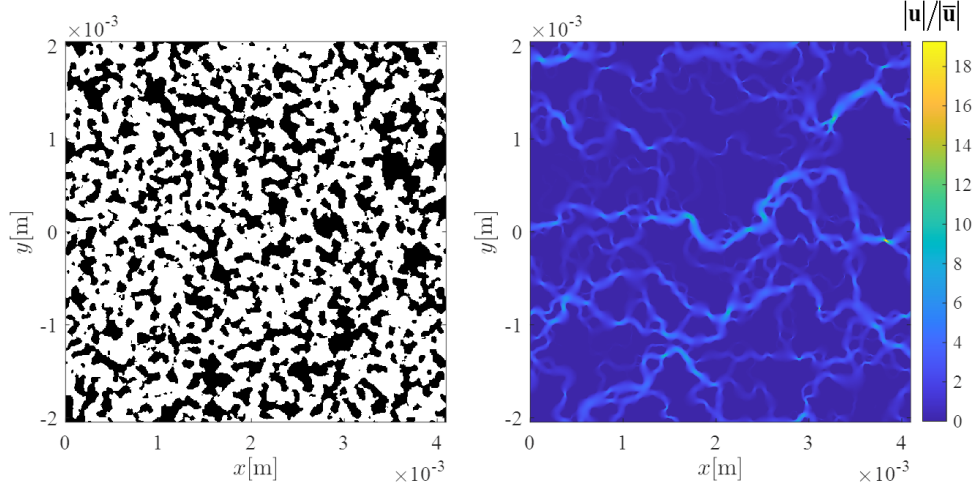


Figure 1: Geometry (left) and normalized velocity magnitude $|\mathbf{u}|/|\bar{\mathbf{u}}|$ (right) in the unit cell.

123 field I , with $I = 1$ associated with pore space and $I = 0$ with solid pixels. The
 124 correlation length of the indicator field I is taken as a representative length
 125 scale for the pore space and is denoted as ℓ_S . Transport is described by the
 126 standard advection-diffusion equation with no flux boundary conditions at
 127 the solid-fluid interface

$$\begin{aligned}
 \frac{\partial C(\mathbf{x}, t)}{\partial t} + \nabla \cdot [\mathbf{u}(\mathbf{x})C(\mathbf{x}, t)] &= \nabla \cdot [D\nabla C(\mathbf{x}, t)] \quad \forall \mathbf{x} \in \Gamma_{fluid}, t > t_0 \\
 D \frac{\partial C(\mathbf{x}, t)}{\partial n} &= 0 \quad \forall \mathbf{x} \in \Sigma_{surface}, t > t_0 \\
 C(\mathbf{x}, t_0) &= C_0
 \end{aligned} \tag{2}$$

128 where $\mathbf{u} = [u, v]$ is the fluid velocity, C is solute concentration, D is the
 129 diffusion coefficient, C_0 is the initial concentration distribution. The ve-
 130 locity \mathbf{u} is obtained by numerically solving the Navier-Stokes equations with

131 OPENFOAM®[®], release v1712 [34] and diffusion is assumed to be known and
 132 constant. The velocity is computed assuming periodic boundary conditions
 133 on the cell boundaries and the no slip condition on the fluid-solid interface.
 134 We impose a uniform pressure gradient along the x -direction, labeling x, y
 135 as longitudinal and transverse directions, respectively. The Péclet number
 136 associated with transport is calculated as $Pe = U\ell_S/D$, where U is the av-
 137 erage fluid velocity. In our simulation we set $D = 10^{-9}$ m²/s and we adjust
 138 Pe by setting U to the desired value. Note that this is acceptable as our
 139 simulations are in a Stokes regime, where inertial effects are negligible with
 140 respect to viscous ones. Transport is solved numerically using a Lagrangian
 141 particle based random walk method, where the solute plume is discretized
 142 into a finite number of N particles. Each particle displaces according to

$$\begin{aligned}
 x_i^{n+1} &= x_i^n + u_i dt + \xi_i \sqrt{2Ddt} \\
 y_i^{n+1} &= y_i^n + v_i dt + \eta_i \sqrt{2Ddt}
 \end{aligned}
 \quad i = 1, \dots, N, \quad (3)$$

143 where dt is a time step that is constant, ξ_i, η_i are independent identically
 144 distributed random numbers drawn from normal distributions with zero mean
 145 and unit variance. We define a reference time step dt^* according to the
 146 following criterion $|\mathbf{d}_{max}| \leq 0.5\Delta$ where

$$|\mathbf{d}_{max}| = \max(|\mathbf{u}|) dt + 2\sqrt{2Ddt^*} \quad (4)$$

147 is an estimate of the maximum displacement. No flux boundary conditions
 148 at the fluid-solid boundary are imposed as elastic reflections.

149 *2.2. Spatial Markov Model*

150 We upscale transport using the framework of the trajectory-based spatial
151 Markov model proposed in [30]. The methodology is based upon pore scale
152 transport trajectories and their associated travel times. In the following, we
153 first describe the pore scale trajectories simulations and then how these are
154 used to parameterize the tSMM.

155 *2.2.1. Pore scale trajectories*

156 Parameterization of the model is grounded on the pore scale simulation of
157 a set $S = \{s_1, \dots, s_{N_s}\}$ of N_s advective-diffusive trajectories, for a specific Pe .
158 These particle trajectories are simulated by solving Eq. (3) across a single
159 cell in the longitudinal direction, i.e., between the inlet location $x = 0$ and
160 the outlet location $x = L_x$. Figure 2 represents a sample of 100 trajectories
161 across the considered unit cell selected from a flux weighted initial condition
162 and setting initial location of particles distributed along the entire unit cell
163 cross section.

164 For each trajectory s_i we record the travel time τ needed to travel across a
165 distance L_x in the longitudinal direction and the y positions (y_{in}, y_{out}) of the
166 particle at the inlet and outlet as the particle enters and exits the domain.
167 Particles are injected at locations $x = 0, y_{in} \in [-L_y/2, L_y/2]$. Particles may
168 cross into adjacent cells along the y direction, but due to the periodicity
169 of the cell geometry each location y_{out} can be mapped to a corresponding
170 \hat{y}_{out} using Eq. (1). Therefore, the coordinate $y_{out}(s_i)$ can be determined as
171 $y_{out}(s_i) = \hat{y}_{out}(s_i) + \Delta_C(s_i)L_y$ where $\Delta_C(s_i)$ is an integer that indicates the
172 net number of cell transitions in the transverse direction observed for a given
173 s_i trajectory path. We can then compute $\Delta y(s_i) = y_{out}(s_i) - y_{in}(s_i)$. The

174 trajectories are subdivided into N_B equiprobable bins that are assigned by
 175 considering the starting locations $y_{in}(s_i)$ in ascending order. This implicitly
 176 defines a discretization of the \hat{y} axis in terms of the binning of the trajectories.
 177 To exemplify this binning, the trajectories in Figure 2 are subdivided into 10
 178 bins, indicated by different colours. The trajectories s_i consider all simulated
 179 pathways between the locations $x = 0, y_{in} \in [-L/2, L_y/2]$ and $x = L_x, y_{out} \in$
 180 $(-\infty, +\infty)$. We observe that some trajectories may even travel backwards
 181 along x close to the inlet section before traveling downstream, as indicated
 182 in the highlighted parts in Figure 2. These effects are due to the combined
 183 action of advection and diffusion and are present for both the considered Pe .
 184 The comparison between the two considered cases allows for identification
 185 of the effects of diffusion on the pore scale trajectory paths. In particular,
 186 for $Pe = 100$ particles explore a wider portion of the pore space than for
 187 $Pe = 1000$.

188 2.2.2. The tSMM parameterization

189 The information collected in the parameterization step is then used to
 190 build the following trajectory-based Spatial Markov model (tSMM)

$$\begin{aligned}
 x_i^{k+1} &= (k + 1)L_x \\
 y_i^{k+1} &= y_i^k + \Delta y [s_i^k | \hat{y}_{out}(s_i^{k-1})] \\
 t_i^{k+1} &= t_i^k + \tau [s_i^k | \hat{y}_{out}(s_i^{k-1})]
 \end{aligned} \tag{5}$$

191 where both y_i^{k+1} and τ_i^{k+1} are determined through a Markov chain, which is
 192 related to the transverse location assigned to the particle in the periodic cell

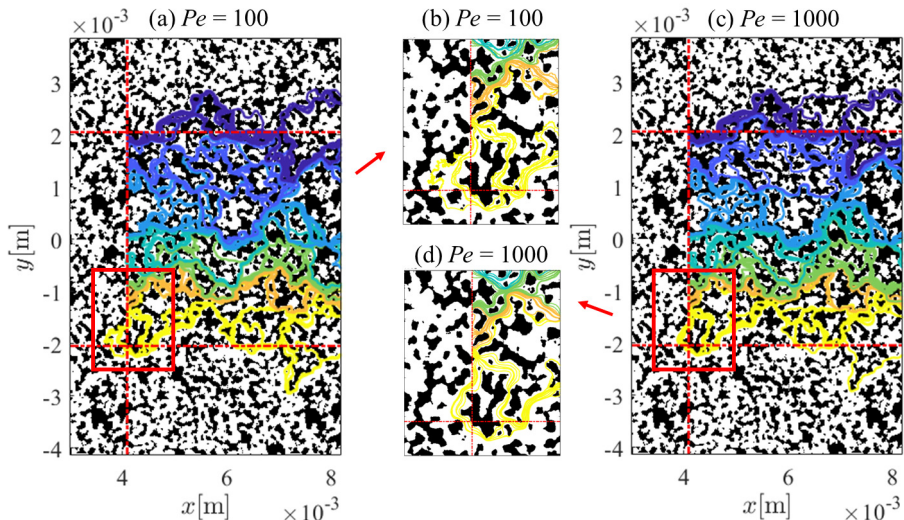


Figure 2: Sample of 100 trajectories employed for model parameterization for (a), (b) $Pe = 100$ and (c), (d) $Pe = 1000$, dashed red lines indicate the unit cell boundaries, the trajectories are binned in different colours as a function of the y_{in} location. The two middle panels represent a zoom on the region highlighted in red for the two cases.

193 during successive steps k , leveraging the information given by the trajectories
 194 in s_i . The innovative feature of the model in Eq. (5) with respect to previous
 195 implementations [30, 21] is that it allows for predictions of transverse spread-
 196 ing over successive Markov steps. This is achieved by considering y as a con-
 197 tinuous variable, i.e., the Markov chain has a longitudinal fixed spatial step
 198 L_x while transport along y is considered through the $\Delta y(s_i)$ obtained from
 199 the trajectories s_i recorded during the parameterization stage. In essence, at
 200 the beginning of the simulation (step $k = 0$) each particle i is assigned to an
 201 initial location y_i^0 corresponding to a selected initial or boundary condition
 202 (e.g., flux weighted or uniform distribution on the inlet boundary). From
 203 this information we select a trajectory s_i^1 , randomly sampling from those
 204 whose $y_{in}(s_i)$ lies in the same bin interval as y_i^0 . By selecting the trajectory

205 we also obtain a given travel time $\tau(s_i^1)$ and transverse displacement $\Delta y(s_i^1)$,
 206 from which we evaluate $\hat{y}_{out}(s_i^1)$. The latter can be then used to select a new
 207 trajectory s_i^2 for the next transition and the procedure can then be repeated
 208 for any arbitrary step number $k > 0$.

209 2.3. Model outputs

210 To analyze the outputs of our tSMM model, our analysis relies on the
 211 following dimensionless space-time coordinates

$$\tilde{x} = \frac{x^k}{L}, \quad \tilde{y} = \frac{y_c}{L}, \quad \tilde{t} = \frac{tU}{L} \quad (6)$$

212 where $L = L_x = L_y$, x^k corresponds to the longitudinal spatial coordinate
 213 of k^{th} Markov step (see Eq. (5)) and $y_c(x) = y(x) - \bar{y}(x)$, i.e., is the trans-
 214 verse location centered with respect to the average transverse position $\bar{y}(x)$
 215 observed at a given x . The value of $\bar{y}(x)$ is not constant with x because the
 216 average transverse velocity component is not exactly equal to zero. While
 217 this component is only approximately 1% of the longitudinal mean velocity
 218 U , it still induces plume migration along y after a number of cells.

219 The key output of the tSMM is the joint probability distribution $P(\tilde{x}, \tilde{y}, \tilde{t})$.
 220 In this distribution, the variable \tilde{x} can only assume discrete values, while the
 221 \tilde{y}, \tilde{t} are continuous.

222 Physically meaningful information related to the plume can then be ex-
 223 tracted from this joint probability by considering conditional and marginal
 224 distributions. In our analysis we will consider the conditional distributions
 225 $P(\tilde{t}, \tilde{y}|\tilde{x})$ for a given dimensionless downstream distance \tilde{x} , or $P(\tilde{x}, \tilde{y}|\tilde{t})$ for
 226 a given dimensionless time, \tilde{t} . Examples of these conditional distributions

227 $P(\tilde{t}, \tilde{y}|\tilde{x})$ for $\tilde{x} = 5, 10, 25$ and 50 and $P(\tilde{x}, \tilde{y}|\tilde{t})$ for $\tilde{t} = 20$, obtained from the
 228 tSMM are shown in Figure 3a and b for $Pe = 100$ and 1000 , respectively.

229 In addition, we consider the marginal probability distributions $P(\tilde{x}, \tilde{y})$,
 230 and $P(\tilde{t}|\tilde{x})$, $P(\tilde{y}|\tilde{x})$ conditional to a given dimensionless downstream distance.
 231 These distributions have a clear physical meaning: the marginal distribution
 232 $P(\tilde{x}, \tilde{y})$ represents the steady state distribution of the particle plume, while
 233 $P(\tilde{t}|\tilde{x})$ corresponds to the breakthrough curve, i.e., the first passage time
 234 probability distribution at distance \tilde{x} . Finally, the probability distribution
 235 $P(\tilde{y}|\tilde{x})$ provides the probability distribution associated with transverse po-
 236 sition at a control plane and is related solely to transport in the transverse
 237 direction.

238 To produce benchmark data against which to test the tSMM we run
 239 a 50 cell high resolution random walk direct numerical simulation (DNS)
 240 using transport Eq. (3). The accuracy of the tSMM defined in section 2.2
 241 will be tested by comparing the above mentioned probability distributions
 242 with their analogs obtained from the DNS. For each of the above defined
 243 distributions we provide a quantitative evaluation of the mismatch between
 244 DNS and tSMM using the Hellinger distance [35]

$$HD[F_1, F_2] = \frac{1}{\sqrt{2}} \sqrt{\sum_{i=1}^N (\sqrt{f_{1,i}} - \sqrt{f_{2,i}})^2} \quad (7)$$

245 where F_1 is any of the above-mentioned marginal or conditional distribu-
 246 tions predicted by DNS and F_2 corresponds to its counterpart obtained with
 247 the tSMM. These distributions are approximated through N discrete bins
 248 and $f_{1,i}$, $f_{2,i}$ are the values of the distributions in the i^{th} bin.

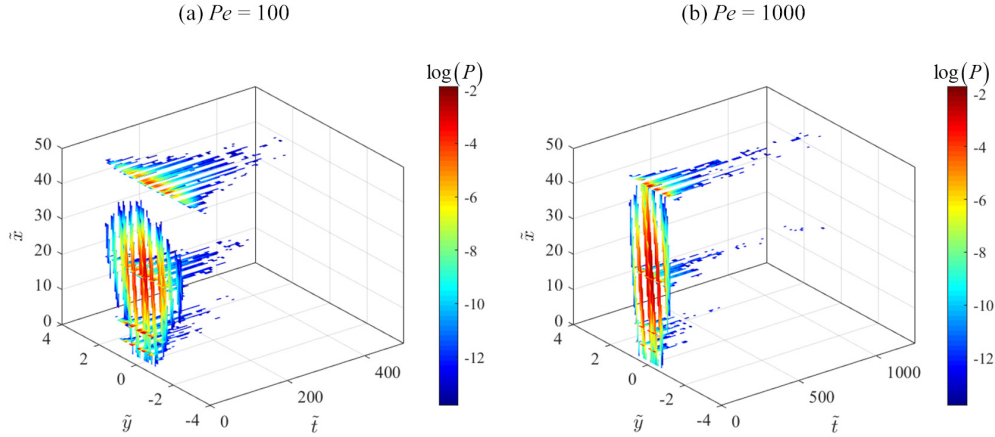


Figure 3: Conditional joint distributions $P(\tilde{t}, \tilde{y}|\tilde{x})$ for $\tilde{x} = 5, 10, 25, 50$ and $P(\tilde{x}, \tilde{y}|\tilde{t})$ for $\tilde{t} = 20$ predicted by the tSMM considering (a) $Pe = 100$ and (b) $Pe = 1000$

249 The HD metric quantifies the distance between two probability measures
 250 and it is a proper distance metric in the mathematical sense, by satisfying
 251 the properties of non-negativity, symmetry, and triangle inequality. HD is
 252 also bounded between 0 and 1, where 0 means that the two distributions are
 253 indiscernible and 1 that they are maximally distant.

254 3. Results

255 First we show results obtained considering parameterization of the tSMM
 256 with $N_s = 10^6$, $N_B = 100$, $dt^* = 10^{-5}$ s and 10^{-6} s for $Pe = 100$ and
 257 $Pe = 1000$, respectively. The time step dt^* indicates the values of dt eval-
 258 uated according to Eq. (4). Then, in section 3.3 we analyze the impact of
 259 parameters N_B and dt on the accuracy of the tSMM. For all cases, including
 260 the DNS reference simulation and tSMM, we impose a flux weighted bound-
 261 ary conditions. Note that In the reference DNS simulation the dt parameter
 262 is kept constant and equal to dt^* .

263 *3.1. Model performance as a function of Pe*

264 The tSMM is able to replicate the shape of the reference conditional dis-
 265 tribution $P(\tilde{t}, \tilde{y}|\tilde{x})$ obtained from the DNS for both investigated Péclet num-
 266 bers. Figure 4a shows the joint distribution $P(\tilde{t}, \tilde{y}|\tilde{x})$ for $\tilde{x} = 25$ and $Pe = 100$
 267 from the high resolution direct numerical simulations and corresponding re-
 268 sults obtained with the tSMM (Figure 4b). The agreement between the two
 269 solutions is significant for all transverse coordinates, \tilde{y} , and dimensionless
 270 travel times, \tilde{t} . Analogous results are obtained for $Pe = 1000$ (see Figure 4c
 271 and d) and for all other investigated Markov steps (not shown). For both Pe
 272 values the maximum value of the probability distributions is found at $\tilde{y} \approx 0$.
 273 Note that \tilde{y} locations associated with zero probability across the whole time
 274 window correspond to the occurrence of solid along the considered transverse
 275 section.

276 To quantify the accuracy of the tSMM outputs with respect to the ref-
 277 erence DNS, Figure 5 shows the metric $HD[P_{DNS}(\tilde{y}, \tilde{t}|\tilde{x}); P_{tSMM}(\tilde{y}, \tilde{t}|\tilde{x})]$ de-
 278 fined in Eq. (7) for both investigated Pe numbers and all Markov steps. We
 279 note that the distance between the DNS and the tSMM distributions slightly
 280 increases with \tilde{x} and is generally larger for $Pe = 100$ than for $Pe = 1000$.
 281 This result is likely due to the fact that the effect of noise in low probability
 282 values increases with the strength of diffusion.

283 Figure 6 depicts conditional joint distribution $P(\tilde{x}, \tilde{y}|\tilde{t})$ for $\tilde{t} = 20$, corre-
 284 sponding to the time dependent solute plume. DNS and tSMM predictions
 285 are shown for $Pe = 100$ (see Figure 6a, b) and for $Pe = 1000$ (see Figure
 286 6c, d). Again, the tSMM is able to capture all essential features displayed
 287 by the fully resolved simulations. Note that tSMM allows for predictions

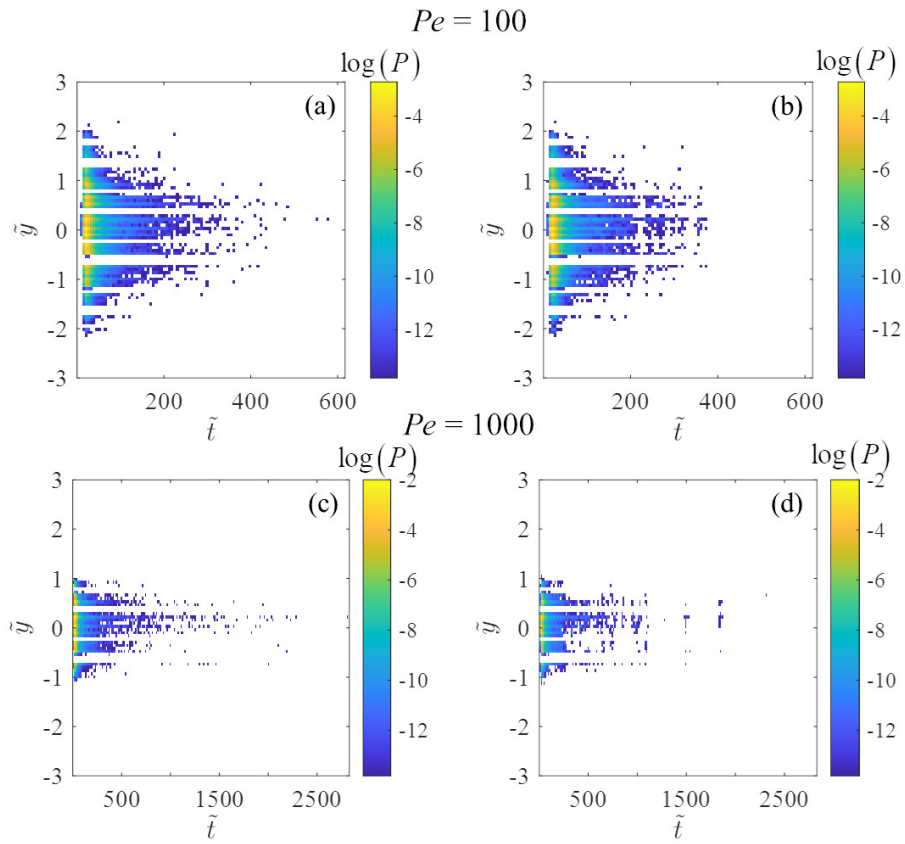


Figure 4: Conditional joint distributions $P(\tilde{t}, \tilde{y} | \tilde{x})$ for $\tilde{x} = 25$ and $Pe = 100$ obtained with (a) DNS, (b) tSMM and for $Pe = 1000$ predicted by (c) DNS and (d) tSMM.

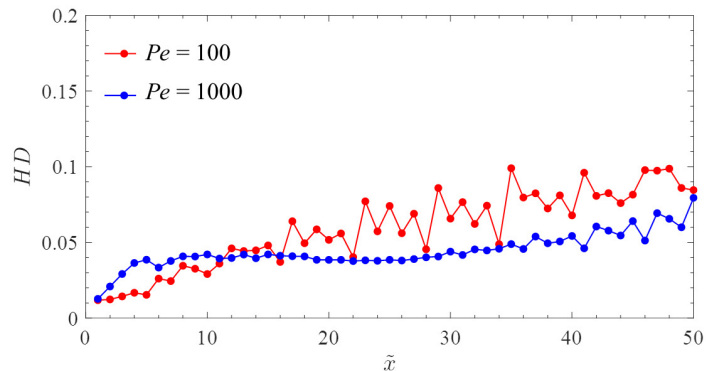


Figure 5: $HD[P_{DNS}(\tilde{y}, \tilde{t}|\tilde{x}); P_{tSMM}(\tilde{y}, \tilde{t}|\tilde{x})]$ as a function of the downstream location \tilde{x} for $Pe = 100$ (red) and 1000 (blue).

288 of the evolution of the plume in the longitudinal and transverse directions
 289 employing a significantly smaller computational effort than the DNS. As an
 290 example, the computational time for running the tSMM is approximately 1%
 291 of that one needed for the DNS results when considering 50 Markov steps.
 292 Note that this percentage decreases for simulation across higher numbers of
 293 unit cells (i.e., the computational gain increases with the dimension of the
 294 system of interest).

295 The marginal distributions $P(\tilde{x}, \tilde{y})$ are depicted in Figure 7a and b for
 296 $Pe = 100$ and 1000 respectively. As mentioned above, these distributions
 297 identify the steady-state plume for a nonreactive solute. These distributions
 298 are here obtained at no additional computational cost with respect to the
 299 transient case, which for a DNS would not be the case and significant addi-
 300 tional cost would be required.

301 Figure 8 displays breakthrough curves $P(\tilde{t}|\tilde{x})$ considering travel distances
 302 $\tilde{x} = 5, 10, 25$ and 50 from the injection location and provides a quantitative
 303 comparison between the reference DNS and the tSMM results. We note that

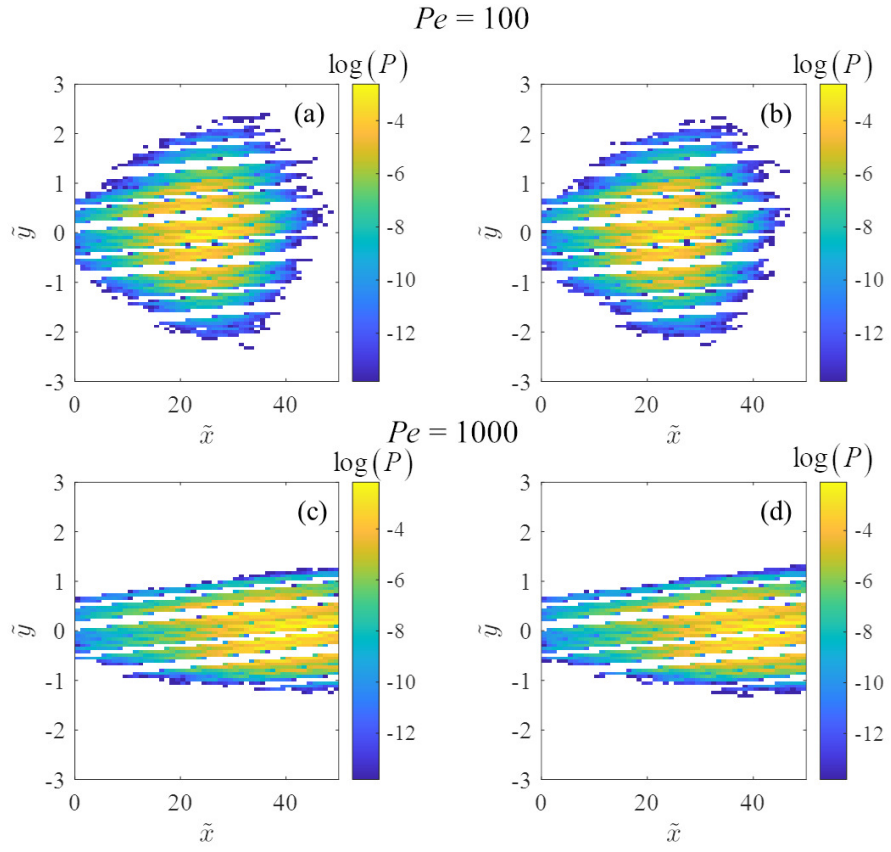


Figure 6: Conditional distributions $P(\tilde{x}, \tilde{y}|\tilde{t})$ for $\tilde{t} = 20$ and $Pe = 100$ obtained with (a) DNS (b) tSMM and for $Pe = 1000$ predicted by (c) DNS and (d) tSMM

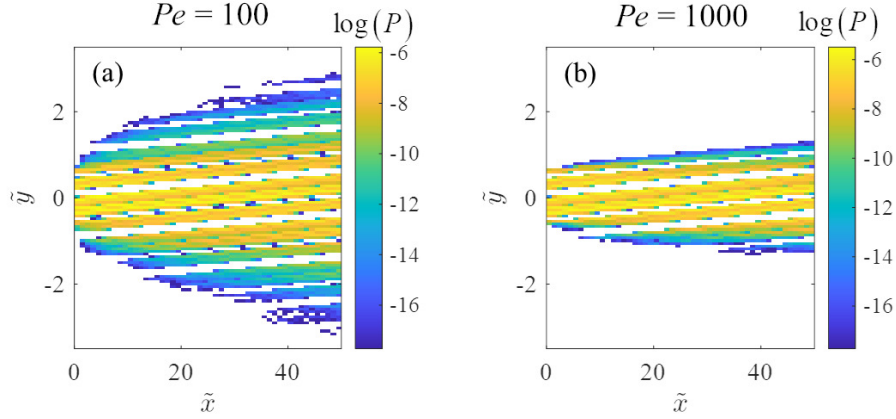


Figure 7: Marginal distribution $P(\tilde{x}, \tilde{y})$ for (a) $Pe = 100$ and (b) $Pe = 1000$.

304 the tSMM can reproduce the breakthrough curves across a wide range of
 305 distances and both Péclet numbers. This result shows that the trajectory-
 306 based upscaled model accurately predicts arrival times in a porous medium
 307 made of periodic unit cells displaying a disordered geometry and is in line
 308 with those obtained within simpler geometrical settings [30].

309 The comparison between tSMM and DNS marginal distribution of trans-
 310 verse locations $P(\tilde{y}|\tilde{x})$ is shown in Figure 9 for two selected distances from
 311 the injection ($\tilde{x} = 5$ and $\tilde{x} = 25$) and for both investigated Pe numbers.
 312 To compare the spreading of the particle plume over all Markov steps we
 313 consider the standard deviation of distribution $P(\tilde{y}|\tilde{x})$ as a function of \tilde{x} (see
 314 Figure 10).

315 Results obtained through the tSMM are in close agreement with those
 316 yielded by the DNS. We observe that the change in Pe has marked effects on
 317 transverse spreading of the solute, as has been previously observed in labora-
 318 tory and numerical studies [10, 13]. In particular, the standard deviation σ_y

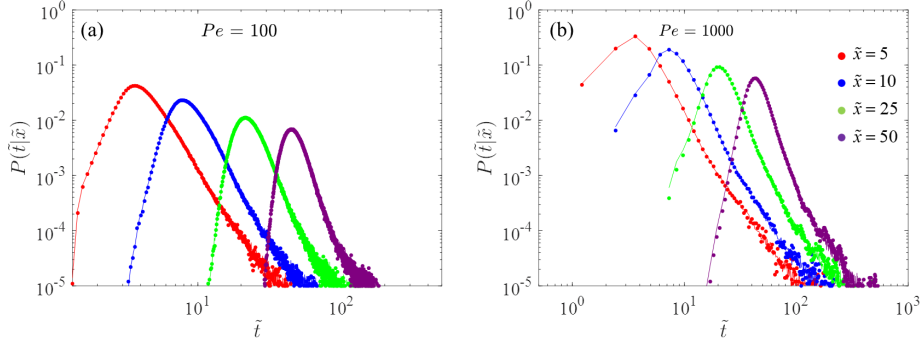


Figure 8: Breakthrough curves $P(\tilde{t}|\tilde{x})$ obtained at control planes located at distances $\tilde{x} = 5, 10, 25, 50$ unit cells for (a) $Pe = 100$ and (b) $Pe = 1000$. Symbols and lines represent the DNS and tSMM results, respectively.

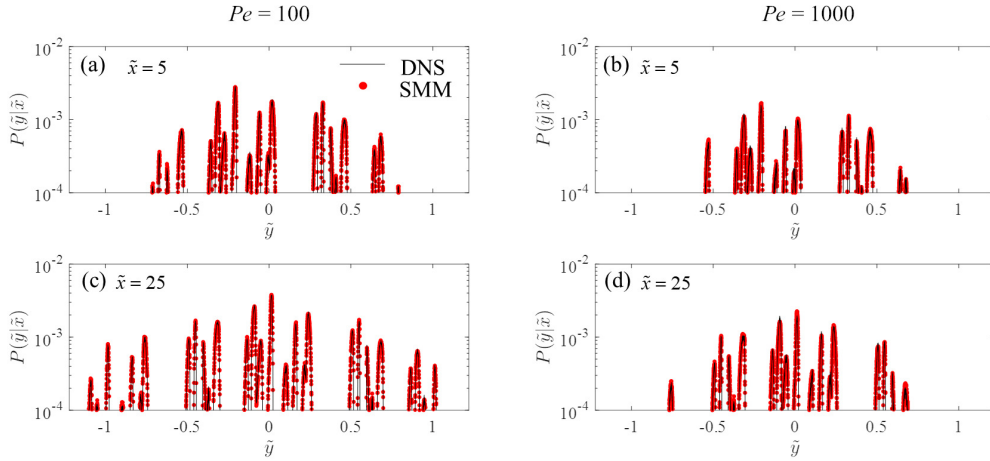


Figure 9: Comparison between the marginal distributions $P(\tilde{y}|\tilde{x})$ as given by direct numerical simulation (black lines) and tSMM (red dots) for $\tilde{x} = 5$ and a) $Pe = 100$, b) $Pe = 1000$, for $\tilde{x} = 25$ and c) $Pe = 100$ and d) $Pe = 1000$.

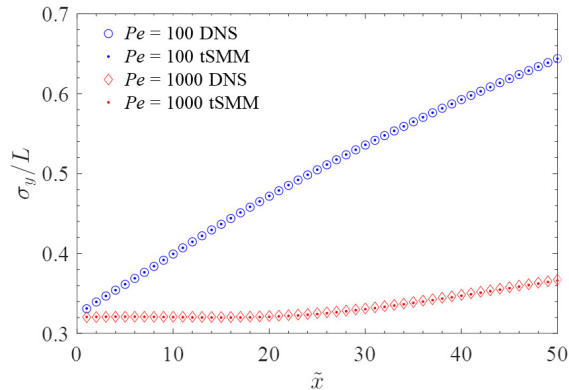


Figure 10: Comparison of the standard deviation, σ_y , of the distribution $P(\tilde{y}|\tilde{x})$ for the DNS and tSMM as a function of \tilde{x} .

319 continuously increases as a function of the longitudinal distance traveled for
 320 $Pe = 100$. On the contrary, σ_y is approximately constant up to $\tilde{x} = 20$ for
 321 $Pe = 1000$ and then starts increasing. This result implies that for such an
 322 advection-dominated situation we only observe significant transverse spread-
 323 ing after particles have traveled a distance of 20 cells. This result is due to
 324 the converging-diverging nature of advective streamlines in two-dimensional
 325 fields, and this particular behavior might be different if investigated in three-
 326 dimensions. Yet, the tSMM is able to predict these different dynamics based
 327 on the simulation of transport across a single unit cell. Note also that the
 328 methodology can be extended to three dimensions, upon relying on the same
 329 procedure described in Section 2.2.

330 3.2. Steady state plumes with first order degradation

331 As a showcase application of the capabilities of the tSMM, we also eval-
 332 uate the influence of a first order reaction on pinching off the steady-state
 333 plume. We assume in this application that the solute undergoes degrada-

334 tion following linear kinetics. This is accounted for in a straightforward
 335 manner in the tSMM framework. Starting from the conservative plume re-
 336 sults (see Figure 7), for each particle we define the probability of reaction as
 337 $R_i(t, \lambda) = 1 - e^{-\lambda t}$, where λ is the kinetic degradation rate. Then we compare
 338 R_i with a random number, U_i , drawn from a standard uniform distribution.
 339 If $U_i \geq P_i$ no reaction occurs while if $U_i < P_i$ the particle is removed from
 340 the system. In our examples λ is chosen based on obtaining specific values
 341 of Damkhöler numbers, $Da = \frac{\ell_s^2 \lambda}{D}$.

342 We compute marginal distributions $P(\tilde{x}, \tilde{y})$ to represent the steady state
 343 plume for this reactive scenario. The results obtained for $Da = 1$ and 5
 344 (corresponding to $\lambda = 0.1$ and 0.5) and $Pe = 100$ are depicted in Figures 11a
 345 and b while Figures 11c and d show the case associated with $Da = 5$ and 10
 346 (corresponding to $\lambda = 0.5$ and 1) and $Pe = 1000$. These results portray the
 347 ability of our proposed tSMM to predict transport in longitudinal and trans-
 348 verse direction while also accounting for a reactive solute undergoing a first
 349 order reaction process. Note that the results are obtained at negligible addi-
 350 tional computational cost with respect to the unsteady state, conservative,
 351 transport simulations.

352 3.3. Error analysis

To provide a quantitative description of the influence of parameters N_B
 and dt on the accuracy of the proposed spatial Markov model we evaluate
 $HD[F_1, F_2]$, see Eq. 7, choosing as F_1 and F_2 the marginal distributions of
 travel times, $P(\tilde{t}|\tilde{x})$, or transverse positions, $P(\tilde{y}|\tilde{x})$, conditional to a given
 downstream location \tilde{x} from the injection point, evaluated with DNS and
 tSMM respectively. Note that the time step is kept constant and equal to

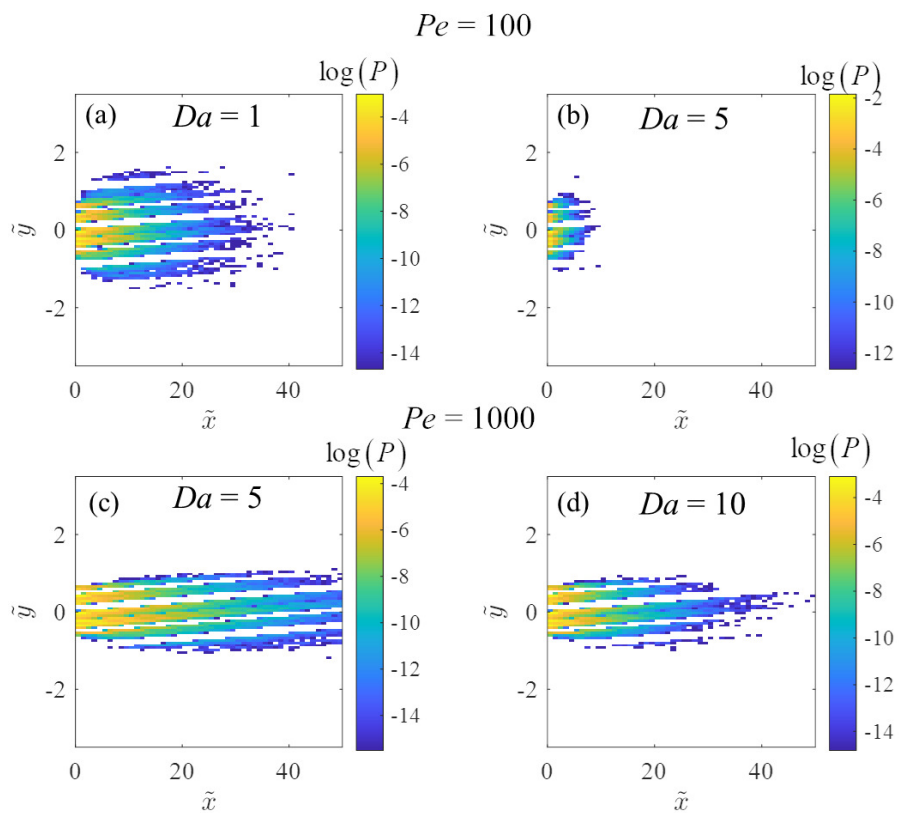


Figure 11: Marginal distribution $P(\tilde{x}, \tilde{y})$ for a reactive contaminant undergoing a degradation following a linear kinetics for $Pe = 100$ (a) $Da = 1$, (b) $Da = 5$, and $Pe = 1000$ (c) $Da = 5$, (d) $Da = 10$.

dt^* in the DNS, while we consider in following different values for the simulation of the trajectories employed to parameterize the tSMM, To simplify the notation we introduce here the following indicators

$$HD_t = HD[P_{DNS}(\tilde{t}|\tilde{x}); P_{SMM}(\tilde{t}|\tilde{x})] \quad (8)$$

$$HD_y = HD[P_{DNS}(\tilde{y}|\tilde{x}); P_{SMM}(\tilde{y}|\tilde{x})] \quad (9)$$

353 to assess the model errors. The analysis is performed considering both
 354 $Pe = 100$ and $Pe = 1000$ and considering different values of N_B and dt
 355 for the parameterization of the tSMM, while, as mentioned above, in the ref-
 356 erence DNS the dt is constant and equal to dt^* . In order to provide an overall
 357 assessment of the impact of parameters dt and N_B we focus on the average
 358 of HD_α (with $\alpha = t, y$) across all 50 investigated Markov steps (the averag-
 359 ing operator is denoted by the symbol $\langle \cdot \rangle$). Figures 12a and b show $\langle HD_t \rangle$
 360 and $\langle HD_y \rangle$ as a function of dt/dt^* and N_B , respectively. Continuous lines
 361 correspond to $Pe = 100$, while dashed lines depict results associated with
 362 $Pe = 1000$. Red and blue colors are related to arrival time and transverse
 363 location distributions, respectively. Note that for $Pe = 100$ both $\langle HD_t \rangle$ and
 364 $\langle HD_y \rangle$ are not very sensitive to the choice of parameter dt (see Figure12a).
 365 On the contrary for $Pe = 1000$ we observe a sharp increase of $\langle HD_t \rangle$ and
 366 $\langle HD_y \rangle$ for $dt > 2dt^*$. This is probably due to the fact that advective particle
 367 displacements depend linearly on dt , as opposed to the diffusive ones which
 368 scale with $dt^{0.5}$. The variation of $\langle HD_t \rangle$ and $\langle HD_y \rangle$ as a function of N_B are
 369 displayed in Figure 12b for the two investigated Pe numbers. These results
 370 show that the quality of model predictions deteriorates for decreasing num-

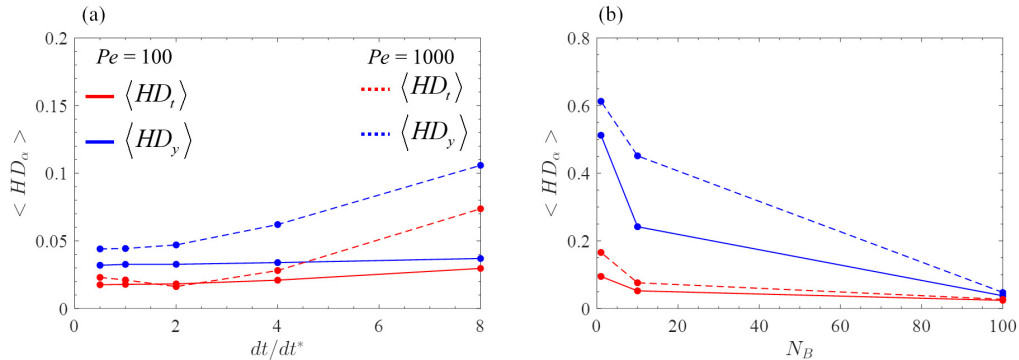


Figure 12: $\langle HD_\alpha \rangle$ for $Pe = 100$ and $Pe = 1000$ as a function of the Markov step number (cell number) for different dt and numbers of bins N_B employed in the parameterization step.

371 ber of bins associated with the tSMM parameterization. Note that $N_B = 1$
 372 corresponds to considering the particle trajectories as totally uncorrelated
 373 across successive Markov steps, while setting $N_B > 1$ in the tSMM param-
 374 eterization allows consideration of correlation between particle trajectories
 375 belonging to the same bin. We note that considering uncorrelated particle
 376 trajectories does not provide good agreement between DNS and tSMM dis-
 377 tributions, as indicated by high values of the HD_α metrics. Also in this case
 378 correlation effects at a fixed downstream distance become stronger as Péclet
 379 number increases, in line with the results of previous studies [22, 31].

380 4. Discussion and conclusions

381 Our study proposes a methodology for upscaling solute plumes in peri-
 382 odic porous media through a trajectory based spatial Markov Model. We
 383 extend the work of [30] to the case of a multi-dimensional unsteady solute
 384 transport and exemplify our approach considering a two-dimensional porous
 385 medium with a disordered geometry. Our framework is based on the simula-

386 tion of advection-diffusion random walk particle trajectories across a single
387 periodic flow cell with the aim of predicting transport over a much larger
388 scale. In particular, our analysis explicitly includes the evaluation of the
389 joint space-time probability distributions associated with solute plumes pro-
390 viding an efficient and accurate representation of both transient and steady
391 state transport in porous media for different Pe numbers. Our work leads to
392 the following major conclusions:

- 393 1. From a comparison with high resolution direct numerical simulations
394 we show that the proposed tSMM accurately predicts spatial and tem-
395 poral distributions of a conservative solute plume using information
396 collected from a single cell simulation. The current framework is not
397 restricted to a simplified geometry setting or a particular flow condition,
398 but can be employed to accurately predict multi-dimensional transport
399 in a realistic two-dimensional pore space once the flow field has been
400 evaluated. Note that, in principle our methodology can be used with
401 different type of initial injection condition, e.g. flux-weighted or uni-
402 formly distributed, pulse or continuous injection, and can be extended
403 to a three-dimensional setup.
- 404 2. Our model is able to predict different transport dynamics, particularly
405 regarding the influence of Pe on transverse plume spreading. Our re-
406 sults are in line with previous laboratory and numerical studies [10, 13].
407 In particular, the change in Pe , due to a change in the diffusion coef-
408 ficient of the compound, had marked effects on transverse spreading of
409 the solute and this is well captured by our upscaling approach.
- 410 3. Particle trajectories and associated travel times, which were simulated

411 with the proposed tSMM to predict conservative transport, can be nat-
412 urally extended to simulate reactive transport processes with negligible
413 additional computational cost. As an example, in this work we analyse
414 the influence of a first order kinetic reaction on a steady state plume.
415 To do so our model has been coupled with a probabilistic representation
416 of a linear degradation reaction and applied for several Da numbers.
417 Note that the methodology is already fully compatible with the analy-
418 sis of other types of reactions (e.g. sorption/desorption) as was shown
419 by [31] for an idealized benchmark problem.

420 4. The effect of tSMM parameterization (in particular the parameters
421 dt and N_B) was studied for the two analysed Pe . As expected, the
422 difference between tSMM and DNS distribution both in space and time
423 increases with increasing dt and decreasing N_B respectively. A marked
424 effect of parameterization was observed for $Pe = 1000$ with respect
425 to $Pe = 100$ due to fact that (i) the contribution of the advective
426 transport, which increases with Pe , is more affected by the choice of
427 dt employed in the tSMM parameterization and (ii) the relevance of
428 particle trajectory correlation increases with Pe .

429 For all the above points the simulation time needed for the tSMM is neg-
430 ligible if compared to the one required for high resolution direct numerical
431 simulation. This is one of the great advantages of the proposed tSMM which
432 allows predicts of multi-dimensional transport across large distances (for both
433 conservative and reactive solutes) without the burden of excessive computa-
434 tional resources. Note that, in its current form, the model can be applied
435 to a spatially periodic domain. This restriction is similar to the fact that

436 solving a closure problem on a periodic unit cell is required for many well es-
437 tablished upscaling procedures. At the same time, broadening the scenarios
438 of interest, for example extending the methodology to upscaling transport of
439 a conservative and/or reactive solute in a disordered non periodic porous do-
440 main would constitute additional elements of interest which are compatible
441 with the approach we rest upon. A first attempt in this direction has been
442 provided by [21, 36] obtaining promising results which can be advanced in
443 the context of future investigations.

444 **Acknowledgments**

445 **Data Availability Statement**

446 Data sets for this research are available online at
447 <https://data.mendeley.com/datasets/rzg53tn963/draft>

448 **References**

- 449 [1] A. Scheidegger, Statistical hydrodynamics in porous media, *Journal of*
450 *Applied Physics* 25 (8) (1954) 994–1001. doi:10.1063/1.1721815.
- 451 [2] A. H.-D. Cheng, J. Bear, *Modeling Groundwater Flow and Contaminant*
452 *Transport*, Springer Publishing Company, 2016.
- 453 [3] F. Valdés-Parada, D. Lasseux, F. Bellet, A new formulation of the dis-
454 *persion tensor in homogeneous porous media*, *Advances in Water Re-*
455 *sources* 90 (2016) 70–82. doi:10.1016/j.advwatres.2016.02.012.
- 456 [4] J. Salles, J.-F. Thovert, R. Delannay, L. Prevors, J.-L. Auriault,
457 P. Adler, Taylor dispersion in porous media. determination of the dis-
458 *persion tensor*, *Physics of Fluids A* 5 (10) (1992) 2348–2376.
- 459 [5] B. Berkowitz, A. Cortis, M. Dentz, H. Scher, Modeling non-fickian trans-
460 *port in geological formations as a continuous time random walk*, *Rev.*
461 *Geophys.* 44 (2).
- 462 [6] B. Wood, F. Valdés-Parada, Volume averaging: Local and nonlocal clo-
463 *sures using a green’s function approach*, *Advances in Water Resources*
464 51 (2013) 139–167. doi:10.1016/j.advwatres.2012.06.008.
- 465 [7] Y. Davit, B. D. Wood, G. Debenest, M. Quintard, Correspondence be-
466 *tween one-and two-equation models for solute transport in two-region*
467 *heterogeneous porous media*, *Transport in porous media* 95 (1) (2012)
468 213–238.

- 469 [8] G. Porta, G. Ceriotti, J.-F. Thovert, Comparative assessment of
470 continuum-scale models of bimolecular reactive transport in porous me-
471 dia under pre-asymptotic conditions, *Journal of contaminant hydrology*
472 185 (2016) 1–13.
- 473 [9] O. Cirpka, A. Valocchi, Two-dimensional concentration distribution for
474 mixing-controlled bioreactive transport in steady state, *Advances in Wa-
475 ter Resources* 30 (6-7) (2007) 1668–1679. doi:10.1016/j.advwatres.
476 2006.05.022.
- 477 [10] G. Chiogna, C. Eberhardt, P. Grathwohl, O. Cirpka, M. Rolle, Evidence
478 of compound-dependent hydrodynamic and mechanical transverse dis-
479 persion by multitracer laboratory experiments, *Environmental Science
480 and Technology* 44 (2) (2010) 688–693. doi:10.1021/es9023964.
- 481 [11] Y. Tang, C. Werth, R. Sanford, R. Singh, K. Michelson, M. Nobu, W.-T.
482 Liu, A. Valocchi, Immobilization of selenite via two parallel pathways
483 during in situ bioremediation, *Environmental Science and Technology*
484 49 (7) (2015) 4543–4550. doi:10.1021/es506107r.
- 485 [12] T. Willingham, C. Werth, A. Valocchi, Evaluation of the effects of
486 porous media structure on mixing-controlled reactions using pore-scale
487 modeling and micromodel experiments, *Environmental Science and
488 Technology* 42 (9) (2008) 3185–3193. doi:10.1021/es7022835.
- 489 [13] M. Rolle, D. Hochstetler, G. Chiogna, P. K. Kitanidis, P. Grathwohl,
490 Experimental investigation and pore-scale modeling interpretation of
491 compound-specific transverse dispersion in porous media, *Transport in*

- 492 Porous Media 93 (3) (2012) 347–362. doi:[https://doi.org/10.1016/](https://doi.org/10.1016/j.advwatres.2020.103574)
493 [j.advwatres.2020.103574](https://doi.org/10.1016/j.advwatres.2020.103574).
- 494 [14] M. Muniruzzaman, M. Rolle, Impact of multicomponent ionic transport
495 on ph fronts propagation in saturated porous media, Water Resources
496 Research 51 (8) (2015) 6739–6755. doi:[10.1002/2015WR017134](https://doi.org/10.1002/2015WR017134).
- 497 [15] Y. Ye, G. Chiogna, O. Cirpka, P. Grathwohl, M. Rolle, Experimental in-
498 vestigation of transverse mixing in porous media under helical flow con-
499 ditions, Physical Review E 94 (1). doi:[10.1103/PhysRevE.94.013113](https://doi.org/10.1103/PhysRevE.94.013113).
- 500 [16] J.-L. Auriault, C. Moyne, H. Souto, On the asymmetry of the dispersion
501 tensor in porous media, Transport in Porous Media 85 (3) (2010) 771–
502 783. doi:[10.1007/s11242-010-9591-y](https://doi.org/10.1007/s11242-010-9591-y).
- 503 [17] S. Pride, D. Vasco, E. Flekkoy, R. Holtzman, Dispersive transport and
504 symmetry of the dispersion tensor in porous media, Physical Review E
505 95 (4). doi:[10.1103/PhysRevE.95.043103](https://doi.org/10.1103/PhysRevE.95.043103).
- 506 [18] T. Le Borgne, D. Bolster, M. Dentz, P. Anna, A. Tartakovsky, Effective
507 pore-scale dispersion upscaling with a correlated continuous time ran-
508 dom walk approach, Water Resources Research 47 (12) (2011) W12538.
- 509 [19] P. K. Kang, P. Anna, J. P. Nunes, B. Bijeljic, M. J. Blunt, R. Juanes,
510 Pore-scale intermittent velocity structure underpinning anomalous
511 transport through 3-d porous media, Geophysical Research Letters
512 41 (17) (2014) 6184–6190.
- 513 [20] A. Puyguiraud, P. Gouze, M. Dentz, Stochastic dynamics of lagrangian

- 514 pore-scale velocities in three-dimensional porous media, *Water Re-*
515 *sources Research* doi:10.1029/2018WR023702.
- 516 [21] T. Sherman, E. B. Janetti, G. R. Guédon, G. Porta, D. Bolster, Upscal-
517 ing transport of a sorbing solute in disordered non periodic porous do-
518 mains, *Advances in Water Resources* (2020) 103574 doi:https://doi.
519 org/10.1016/j.advwatres.2020.103574.
- 520 [22] D. Bolster, Y. Méheust, T. Le Borgne, J. Bouquain, P. Davy, Model-
521 ing preasymptotic transport in flows with significant inertial and trap-
522 ping effects—the importance of velocity correlations and a spatial markov
523 model, *Advances Water Resources* 70 (2014) 89–103.
- 524 [23] T. Sherman, A. Foster, D. Bolster, K. Singha, Predicting downstream
525 concentration histories from upstream data in column experiments, *Wa-*
526 *ter Resources Research* (2018) 9684–9694.
- 527 [24] A. Russian, M. Dentz, P. Gouze, Time domain random walks for hydro-
528 dynamic transport in heterogeneous media, *Water Resources Research*
529 52 (5) (2016) 3309–3323. doi:10.1002/2015WR018511.
- 530 [25] E. Wright, N. Sund, D. Richter, G. Porta, D. Bolster, Upscaling mixing
531 in highly heterogeneous porous media via a spatial markov model, *Water*
532 11 (1) (2019) 53.
- 533 [26] M. Schmuck, P. Berg, Effective macroscopic equations for species trans-
534 port and reactions in porous catalyst layers, *Journal of the Electrochem-*
535 *ical Society* 161 (8) (2014) E3323–E3327. doi:10.1149/2.037408jes.

- 536 [27] H. Kim, J. Bae, D. Choi, An analysis for a molten carbonate fuel cell
537 of complex geometry using three-dimensional transport equations with
538 electrochemical reactions, *International Journal of Hydrogen Energy*
539 38 (11) (2013) 4782–4791. doi:10.1016/j.ijhydene.2013.01.061.
- 540 [28] T. Gebäck, A. Heintz, A pore scale model for osmotic flow: Homoge-
541 nization and lattice boltzmann simulations, *Transport in Porous Media*
542 126 (1) (2019) 161–176. doi:10.1007/s11242-017-0975-0.
- 543 [29] F. Municchi, M. Icardi, Macroscopic models for filtration and hetero-
544 geneous reactions in porous media, *Advances in Water Resources* 141
545 (2020) 103605. doi:https://doi.org/10.1016/j.advwatres.2020.
546 103605.
- 547 [30] N. L. Sund, G. M. Porta, D. Bolster, Upscaling of dilution and mixing
548 using a trajectory based spatial markov random walk model in a periodic
549 flow domain, *Advances in Water Resources* 103 (2017) 76–85.
- 550 [31] T. Sherman, A. Paster, G. Porta, D. Bolster, A spatial markov model
551 for upscaling transport of adsorbing-desorbing solutes, *Journal of con-
552 taminant hydrology* 222 (2019) 31–40.
- 553 [32] P. K. Smolarkiewicz, C. L. Winter, Pores resolving simulation of Darcy
554 flows, *Journal of Computational Physics* 229 (9) (2010) 3121–3133.
- 555 [33] J. D. Hyman, C. L. Winter, Stochastic generation of explicit pore struc-
556 tures by thresholding Gaussian random fields, *Journal of Computational
557 Physics* 277 (2014) 16–31.

- 558 [34] OpenCFD Limited, OpenFOAM The Open Source CFD Toolbox, user
559 guide version v1712, <https://www.openfoam.com/>, accessed: 2019-09-
560 29 (2017).
- 561 [35] E. Hellinger, Neue begründung der theorie quadratischer formen von un-
562 endlichvielen veränderlichen., *Journal Für Die Reine Und Angewandte*
563 *Mathematik* (1909) 210–271doi : 10 . 1515/crll . 1909 . 136 . 210 .
- 564 [36] T. Sherman, J. Hyman, M. Dentz, D. Bolster, Characterizing the influ-
565 ence of fracture density on network scale transport, *Journal of Geophys-*
566 *ical Research: Solid Earth* 125 (1) (2020) e2019JB018547.